Atomic-scale modeling of nanostructure formation in Fe–Ga alloys with giant magnetostriction: Cascade ordering and decomposition

Julien Boisse, Helena Zapolsky, Armen G Khachaturyan

Atomic-scale modeling of nanostructure formation in Fe–Ga alloys with giant magnetostriction: Cascade ordering and decomposition

J. Boisse [a], H. Zapolsky [b], A.G. Khachaturyan [a,*]

[a] *Department of Materials Science and Engineering, Rutgers University, 607 Taylor Road, Piscataway, NJ 08854, USA*
[b] *GPM, UMR 6634 CNRS, Avenue de l'Université, 76801 St Etienne du Rouvray, BP 12, France*

The Fe–Ga body-centered cubic (bcc) alloys within the 15–20 at.% Ga composition range have abnormally high magnetostriction. There is growing evidence that this effect is associated with the magnetic field-induced flip of tetragonal axes of nanoparticles of the ordered phase formed in this range. We studied structural transformations within this composition range at 550 °C by using computer modeling of the atomic-scale ordering and clustering in the atomic density field approximation. It is shown that the initial stage of equil-ibration of the compositionally homogeneous bcc solid solution with 19 at.% Ga results in bcc → B2 congruent ordering followed by a precipitation of Ga-rich B2 particles, which eventually transform to particles of the DO_3 phase. At the composition 21 at.% Ga, the con-gruently ordered B2 phase undergoes further B2 → DO_3 congruent ordering, which is followed by decomposition into an equilibrium mixture of the bcc and DO_3 phases. An important result is that the phase transformations at $0.15 < c < 0.19$ produce nanoparticles of transient B2 phase. We assume that the nanoprecipitates of the transient B2 phase undergo a diffusionless cubic → tetragonal trans-formation, forming the $L1_0$ phase during cooling to the room temperature, and that this involves a magnetic field-induced flipping of tetragonality of these nanoprecipitates which may be responsible for the giant magnetostriction.

Keywords: Iron; Gallium; Magnetostriction; Atomic ordering; Atomistic modeling

1. Introduction

Recent observations of giant magnetostriction (GM) in the ferromagnetic body-centered cubic (bcc) phase of Fe–Ga alloys within the composition range 15–20 at.% Ga [1,2] have attracted significant attention. It is interesting that the observed peak of the magnetostriction falls at the solubility limit of the A2 (bcc phase) of the known phase diagram [3] near 19.5 at.% Ga [1]. The diagram presented in Fig. 1 is in fact a metastable phase diagram because the formation of the equilibrium face-centered cubic (fcc)-based $L1_2$ ordered phase below 650 °C [3] is so sluggish that in most cases the decomposition and ordering develop in accordance with the metastable phase diagram shown in Fig. 1. For brevity we will call this diagram the equilibrium phase diagram.

An extrinsic model of observed GM has recently been proposed by Khachaturyan and Viehland (KV) [4,5]. The KV model assumes that the Fe–Ga alloys with GM within the ~15–20 at.% Ga range are, in fact, two-phase dispersions of coherent nanoparticles of the tetragonally distorted phase rather than homogeneous bcc alloys as is usually believed. This assumption is supported by the transmission electron microscopy (TEM) observation of coherent nanoparticles of the second phase in Fe–Ga alloys within the ~15–20 at.% Ga range [6–10]. The observations of nanoprecipitates at concentrations at of least 15 at.% Ga and higher indicate that the solubility limit of the bcc phase should be shifted to at least this composition. It is interesting that coherent nanoprecipitates of the ordered phase have also been observed within the A2 field of the chemically similar Fe–Al system [11,12].

* Corresponding author. Tel.: +1 732 445 4711; fax: +1 732 445 6780.
E-mail address: Khach@jove.rutgers.edu (A.G. Khachaturyan).

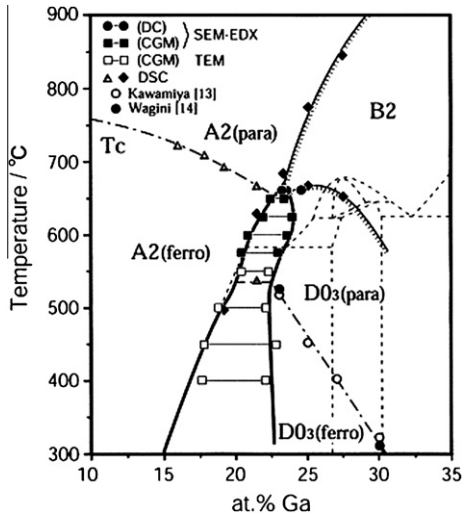

Fig. 1. Fe–Ga metastable phase diagrams from Ref. [3].

Elucidating this nanoprecipitate mechanism of the GM in Fe–Ga alloys requires understanding the atomic-scale and nanoscale structural transformations that occur between 15 and 20 at.% Ga. The latter poses a serious difficulty because the equilibration kinetics in this case should occur via a cascade of congruent ordering (which maintains compositional homogeneity) and decomposition, producing transient phases [13–15]. According to the KV model of GM, the equilibration of the system should also involve the diffusionless cubic → tetragonal transformation in nanoprecipitates upon cooling to room temperature. The possibility of such a transformation and its effect on the magnetostriction will be considered in a subsequent paper.

To investigate the structural effects of atomic ordering and precipitation in Fe–Ga alloys, we carried out a 3-D atomic-scale computational prototyping of these processes within the composition range corresponding to the observed peak of the magnetostriction at the typical temperature 550 °C.

2. Theoretical background

To model the atomic processes during ordering and precipitation, we used the atomic density field (ADF) theory [16–18]. The ADF theory is an atomic-scale phase field theory in which phase fields are atomic occupation density functions. In the case of bcc-based Fe–Ga alloys the density functions, $n(\mathbf{r}, t)_{\mathrm{Fe}}$ and $n(\mathbf{r}, t)_{\mathrm{Ga}}$, are the occupation probabilities of finding Fe and Ga atoms, respectively, at lattice site $\mathbf{r}$ at a given time t. In a binary substitutional solid solution, the density functions $n(\mathbf{r}, t)_{\mathrm{Fe}}$ and $n(\mathbf{r},t)_{\mathrm{Ga}}$ are not independent. They are related by the identity, $n(\mathbf{r})_{\mathrm{Fe}} + n(\mathbf{r})_{\mathrm{Ga}} = 1$. Therefore, the atomic configuration of the system can be fully described by just the density function. For certainty, we assume that this function is $n(\mathbf{r})_{\mathrm{Ga}} = n(\mathbf{r}, t)$. A temporal and spatial dependence of $n(\mathbf{r}, t)$ describes the evolution of the microstructure on the atomic-scale [17,18]:

$$\frac{dn(\mathbf{r},t)}{dt} = \sum_{\mathbf{r}'} L(\mathbf{r},\mathbf{r}')\frac{\partial F(\{n\})}{\partial n(\mathbf{r}',t)}, \tag{1}$$

where $L(\mathbf{r}, \mathbf{r}')$ is the effective rate of elementary diffusion jump between the nearest lattice sites $\mathbf{r}$ and $\mathbf{r}'$, $F(\{n\})$ is a function of the atomic density function, $n(\mathbf{r}, t)$. The summation in Eq. (1) is carried out over all N lattice sites of the crystal. $F = F_{chem} + E_{elast}$ is the total free energy of the system including the chemical and the strain energy contributions. In fact, the kinetic matrix, $L(\mathbf{r} - \mathbf{r}')$, depends on the density field, $n(\mathbf{r})$ [17,18], but at the growth stage this dependence is reduced to a renormalization of the effective values of $L(\mathbf{r} - \mathbf{r}')$. The kinetic Eq. (1) approximates the evolution rate by the first nonvanishing term of its expansion with respect to the thermodynamic driving force, $\frac{\partial F}{\partial n(\mathbf{r}',t)}$ (small driving force). Eq. (1) is significantly nonlinear with respect to the density field, $n(\mathbf{r})$, although it is linear with respect to the driving force.

The chemical free energy of the binary system was interpolated by the equation for the mean field free energy [16–18]:

$$F_{chem} = \frac{1}{2N}\sum_{k} V(\mathbf{k})|\tilde{n}(\mathbf{k})|^2 + k_B T \sum_{r}[n(\mathbf{r})\ln(\mathbf{r}) + (1 - n(\mathbf{r}))\ln(1 - n(\mathbf{r}))], \tag{2}$$

where $\tilde{n}(\mathbf{k}) = \sum_r n(\mathbf{r})\exp(-i\mathbf{k}\cdot\mathbf{r})$ and $V(\mathbf{k}) = \sum_r W(\mathbf{r})\exp(-i\mathbf{k}\cdot\mathbf{r})$ are the Fourier transforms of $n(\mathbf{r})$ and mixing energy $W(\mathbf{r}, t)$; summation over $\mathbf{r}$ is carried out over all N bcc lattice sites; summation over $\mathbf{k}$ is over all points of the quasicontinuum within the first Brillouin zone of the bcc lattice permitted by periodic boundary conditions. Assuming the three-nearest-neighbor approximation for $W(\mathbf{r}, t)$, we have:

$$V(K) = 8w_1(\cos\pi h\cos\pi k\cos\pi l) + 2w_2(\cos 2\pi h + \cos 2\pi k + \cos 2\pi i) + 4w_3(\cos 2\pi h\cos 2\pi k + \cos 2\pi h\cos 2\pi l + \cos 2\pi k\cos 2\pi l), \tag{3}$$

where w_1, w_2 and w_3 are the values of effective interchange interaction energies, $W(\mathbf{r}, t)$, for the first-, second- and third-nearest-neighbors, respectively; (h, k, l) are continuous dimensionless coordinates of the $\mathbf{k}$ vector defined as $\mathbf{k} = (k_x, k_y, k_z) = (2\pi/a)(h, k, l)$, a is the lattice parameter of the underlying bcc lattice.

Eq. (2) is asymptotically accurate at low and high temperatures. It also provides a good interpolation of the free energy of the bcc binary solution at intermediate temperatures. It becomes exact if the mixing energies of Eq. (3) are presented as functions of temperatures and composition [17]. We increased this accuracy considering the mixing energies as input parameters that are determined by fitting to the known phase diagram [3] at the modeling temperature 550 °C within the range of composition under investigation.

To calculate the phase diagram using Eq. (2), we have employed the static concentration wave method [16–18].

In the concentration wave representation a general equation for the density function, $n(\mathbf{r})$, describing the atomic distribution of Ga atoms in all phases in the Fe-rich part of the phase diagram is:

$$n(\mathbf{r}) = c - x\exp(i\mathbf{k}_0\cdot\mathbf{r}) + y\left(\frac{1}{2i}\exp(i\mathbf{k}_1\cdot\mathbf{r}) - \frac{1}{2i}\exp(-i\mathbf{k}_1\cdot\mathbf{r})\right) = c - x\exp(i\mathbf{k}_0\cdot\mathbf{r}) + y\sin(\mathbf{k}_1\cdot\mathbf{r}), \quad (4)$$

where vectors: $\mathbf{k}_0 = \frac{2\pi}{a}(1\,1\,1)$ and $\mathbf{k}_1 = \frac{2\pi}{a}\left(\frac{1}{2}\,\frac{1}{2}\,\frac{1}{2}\right)$, and $\frac{1}{N}\tilde{n}(\mathbf{k}_0) = x$ and $\frac{1}{N}\tilde{n}(\mathbf{k}_1) = y$ are the amplitudes of the corresponding concentration waves and also are the long-range order parameters. Their equilibrium values are determined by the minimization of the free energy (2). Eq. (4) describes the DO_3 phase if x and y are not zeros. It also describes the B2 ordered phase if $y = 0$ and $x \neq 0$. Then the B2 order is generated by the only wave vector $k_0 = \frac{2\pi}{a}(1\,1\,1)$. Substituting $\frac{1}{N}\tilde{n}(\mathbf{k}_0) = x$ and $\frac{1}{N}\tilde{n}(\mathbf{k}_1) = y$ to the first term in Eq. (2) and taking into account that the other amplitudes are zero, we have:

$$\frac{1}{2N}\sum_k V(\mathbf{k})|\tilde{n}(\mathbf{k})|^2 = \frac{N}{2}\left\{V(\mathbf{0})c^2 + V(\mathbf{K}_0)x^2 + V(\mathbf{k}_1)\frac{y^2}{2}\right\} \quad (5)$$

The dependence of the second term in Eq. (2) on x and y is determined by a substitution of (4) into (2).

A reasonably good fit to the phase diagram is obtained by using the mixing energies: $w_1 = 39.6$ meV, $w_2 = 5.6$ meV and $w_3 = -23.1$ meV. Using these values in Eq. (3) gives $V(\mathbf{0}) = 850\ k_B$, $V(\mathbf{k}_0) = -6500\ k_B$, and $V(\mathbf{k}_1) = -3600\ k_B$. The calculated dependences of the free energies of the A2, B2 and DO_3 phases vs. composition at temperature 550 °C are presented in Fig. 2. The calculated solubility limits for the disordered A2 phase and DO_3 phase are obtained by the common tangent construction for the free energies in Fig. 2. They are ~0.14 and ~0.25, respectively. The calculated second-order A2 → B2 congruent ordering transition at 550 °C—a point of absolute instability of the disordered A2 phase with respect to the congruent B2 order—corresponds to the concentration $c \sim 0.148$. The calculated composition at which the B2 phase becomes unstable with respect to DO_3 ordering at the same temperature is $c \sim 0.197$.

The elastic strain energy contribution to the free energy in Eq. (1) was calculated by using the microelasticity theory [18–20]. We used the concentration coefficient of the crystal lattice expansion, $u = \frac{a_{DO_3}/2 - a_{A2}}{a_{A2}(c_{DO_3} - c_{A2})}$, and the elastic constants c_{11}, c_{12} and c_{44} which characterize crystals of cubic symmetry.

The gray area in Fig. 2 indicates the composition range at a given temperature where the equilibration of the homogeneous bcc solution is expected to start via bcc → B2 congruent ordering. This process reduces the free energy without changing the composition (arrow 1 in Fig. 2) [21,22]. The congruent ordering produces a compositionally homogeneous transient ordered B2 phase but cannot produce the DO_3 phase. The congruent ordering precedes the decomposition because it is the fastest mode of free energy reduction. It requires atomic-scale diffusion while the decomposition requires long-range diffusion.

The calculated metastable "diffusionless" phase diagram describing a conditional equilibrium between the A2, B2 and DO_3 phases at the same composition is shown in Fig. 3. The lines on this phase diagram describe the diffusionless equilibrium between the A2 (bcc), B2 and DO_3 phases. The gray area indicates the T–c field where the congruent ordering of the quenched bcc phase (left vertical arrow) can produce only the B2 phase because the free energy of the B2 phase is lower than the free energy of the DO_3 phase at the same composition. On the other hand a quenching of the bcc phase into the DO_3 phase field, shown by the right vertical arrow, is expected to produce a cascade of bcc → B2 → DO_3 congruent orderings. These orderings produce transient B2 and DO_3 nonstoichiometric phases.

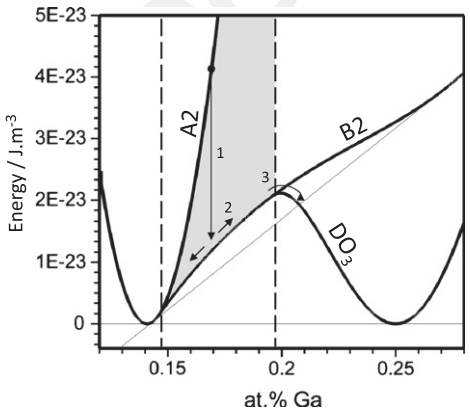

Fig. 2. The calculated free energy vs. composition dependence for the A2, B2 and DO_3 phases at 550 °C. 1, 2 and 3 indicate the three-step decomposition processes involved in quenching the Fe–Ga compound (see text for the details).

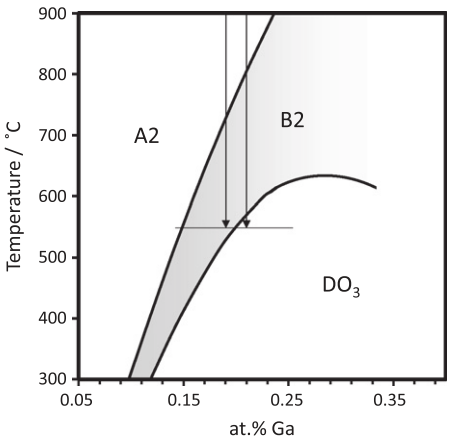

Fig. 3. The calculated diffusionless phase diagram of Fe–Ga alloys. The shadowed area indicates the region of stability of the B2 ordered phase in the absence of decomposition. Two vertical lines illustrate "quenching" of the disordered A2 phase to 550 °C at the alloy composition $c = 0.19$ and $c = 0.21$.

The final bcc + DO_3 equilibrium dictated by the observed phase diagram in Fig. 1 (in fact, it is a metastable phase diagram because it does not takes into account the formation of the stable $L1_2$ phase that kinetically is very sluggish and requires very long annealing) is reached by the decomposition of the transient congruently ordered phases. As has been mentioned above, we call this diagram an equilibrium diagram.

The equilibrium phase diagram calculated with the selected mixing energy used as a fitting parameter, which does not take into account formation of the equilibrium $L1_2$ phase, is shown in Fig. 4. The dashed lines are continuations of the lines of diffusionless equilibrium inside the A2 + DO_3 two-phase field. They are also the lines of the conditional spinodal [23]. The horizontal line indicates the temperature of isothermal "annealing".

3. Computational modeling

To perform computer modeling of atomic ordering and compositional clustering kinetics during the cascade transformation A2 → B2 → DO_3, we solved numerically the atomic density function kinetic equation (Eq. (1)) for occupation density, $n(\mathbf{r}, t)$, where $\mathbf{r}$ indicates the crystal lattice of the underlying bcc lattice. We assume that $L(\mathbf{r}-\mathbf{r}')$ does not vanish only for the nearest-neighbor sites of the bcc lattice, $\mathbf{r}$ and $\mathbf{r}'$, and that it is equal to L_1 where L_1 is the effective rate of the elementary diffusional jumps between the nearest-neighbor sites of the underlying bcc lattice.

In the calculations we used a reduced form of Eq. (1). The reduced time is $t^* = t/\tau$, where $\tau = [L_1 k_B T_0]^{-1}$ is the typical time for an elementary diffusion event. The reduced temperature is $T^* = T/T_0$, where $T_o = 893$ K is chosen as the maximum temperature of the B2 → DO_3 ordering at the stoichiometric composition of the DO_3 phase, $c = 0.25$. All energies are measured in units $k_B T_o$, and the strain energy contribution is determined by the dimensionless parameter $\chi = v(c_{11}+2c_{12})^2 u^2/(c_{11}k_B T_0)$, where

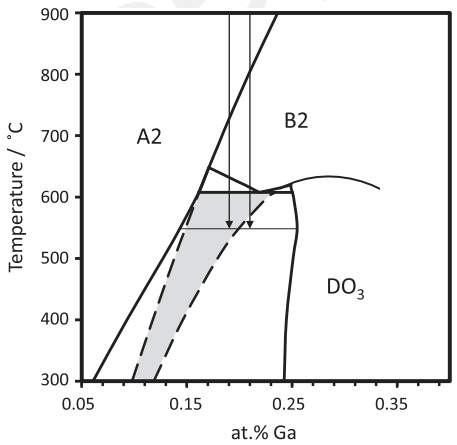

Fig. 4. The calculated "equilibrium" Fe–Ga phase diagram corresponding to the observed diagram shown in Fig. 1. Dashed lines are lines of A2/B2 and B2/DO_3 diffusionless equilibrium.

$u = da/a_0 dc$ is the concentration coefficient of the crystal lattice expansion of the bcc host lattice, $v = a_0^3/2$ is the volume per bcc lattice site. The parameter χ determines the balance between the chemical energy and the elastic energy of the alloy. Then the reduced values of the mixing energies are $w_1^* = w_1/(k_B T_0) = 0.515$, $w_2^* = w_2/(k_B T_0) = 0.0724$ and $w_3^* = w_3/(k_B T_0) = -0.30$. The chosen elastic constants are: $c_{11} = 228$ GPa, $c_{12} = 132$ GPa, $c_{44} = 117$ GPa [24,25]. The lattice parameter of the A2 disordered phase and the ordered DO_3 phase are $a_{A2} = 2.87$ Å at $c_{A2} = 0$ and $a_{DO_3}/2 = 2.9$ Å at $c_{DO_3} = 0.22$ [22], respectively. Then assuming the linear Vegard law for the compositional dependence of crystal lattice parameters, we have $u = 0.049$. The calculated reduced elastic energy parameter is $\chi \sim 2.5$.

The numerical solution of the ADF kinetic Eq. (1) was carried out by using the semi-implicit Fourier-spectral method [21] and periodic boundary conditions. The 3-D simulation box was 128 × 128 × 128 bcc unit cells. A uniform time step of $\Delta t^* = 0.1$ was used. The initial state was a homogeneous disordered bcc solution with small composition fluctuations around the average composition. The obtained microstructures were visualized on the atomic-scale and the nanoscales. A visualization on the atomic-scale was based on imaging of occupation probability, $n(\mathbf{r})$, obtained by numerical solution of Eq. (1). Nanoscale imaging employed the appropriate coarse-graining of $n(\mathbf{r})$. In particular, local coarse-grained values of $x(\mathbf{r})$ and $y(\mathbf{r})$ were defined in terms of occupation densities, $n(\mathbf{r})$, around a site $\mathbf{r}$: they are mean values of $n(\mathbf{r})$ over all sites of a $2a \times 2a \times 2a$ volume of a DO_3 lattice cell, where a is the bcc lattice parameter, with origin of this cell being located in its center at the site $\mathbf{r}$. These local values of $c(\mathbf{r})$, $x(\mathbf{r})$, and $y(\mathbf{r})$ are then defined as:

$$
\begin{aligned}
c(\mathbf{r}) &= \frac{1}{2^4} sum_\rho n(\mathbf{r}+\boldsymbol{\rho}) \\
x(\mathbf{r}) &= \frac{1}{2^4}\sum_\rho n(\mathbf{r}+\boldsymbol{\rho})\exp(-i\mathbf{k}_0\cdot\boldsymbol{\rho}) \\
y(\mathbf{r}) &= \frac{i}{2^3}\sum_\rho n(\mathbf{r}+\boldsymbol{\rho})\exp(-i\mathbf{k}_1\cdot\boldsymbol{\rho}) \quad \text{if} x > 0 \\
y(\mathbf{r}) &= \frac{1}{2^3}\sum_\rho n(\mathbf{r}+\boldsymbol{\rho})\exp(-i\mathbf{k}_1\cdot\boldsymbol{\rho}) \quad \text{if} x < 0
\end{aligned}
\tag{6}
$$

where a summation over vector $\boldsymbol{\rho}$ is carried out over all 16 bcc lattice sites of the $2a \times 2a \times 2a$ bcc double cell volume including the origin at the site $\mathbf{r}$ corresponding to $\boldsymbol{\rho} = 0$.

We also visualized the coordinate dependence of the normalized amplitudes of the concentration wave that are the $x(\mathbf{r})/x_{\max}$ and $y(\mathbf{r})/y_{\max}$ ratios, where $x_{\max}$ and $y_{\max}$ are maximum absolute values of these amplitudes which correspond to the absolute values of x and y determined by the minimization of the free energy (2) describing the DO_3 phase at $c = 0.25$. $x(\mathbf{r})/x_{\max}$ and $y(\mathbf{r})/y_{\max}$ ratios are proportional to the corresponding long-range order parameters of the B2 and DO_3 phases.

4. Modeling results

We modeled equilibration of two homogeneous A2 alloys with compositions of Ga, $c = 0.19$, and $c = 0.21$ "annealed" at $T = 550$ °C. These two choices correspond to two different thermodynamic conditions (two vertical arrows in Fig. 3) and, thus, the equilibration kinetics in these cases is expected to have a different transformation pathway.

Indeed, the point ($T = 550$ °C, $c = 0.19$) is located within the gray area of the diffusionless phase diagram in Fig. 3, and thus an initial diffusionless equilibration of the A2 phase in this case can produce only B2 transient phase in a single-phase off-stoichiometric state. It cannot produce the DO_3 phase—the equilibrium DO_3 phase can be formed only as a result of decomposition of the transient B2 phase. On the other hand, the annealing point ($T = 550$ °C, $c = 0.21$) is located below the gray area of the diffusionless phase diagram in Fig. 3. The diffusionless equilibration in this case allows the formation of the off-stoichiometric DO_3 phase as a result of the secondary ordering within the previously formed B2 phase.

Our solution of Eq. (1) at $T = 550$ °C with compositions $c = 0.19$ and $c = 0.21$ demonstrates that equilibration of the homogeneous bcc solid solution occurs as a cascade process rather than by direct nucleation of the equilibrium DO_3 phase within the supersaturated A2 matrix. The first stage of equilibration is a congruent ordering. It results in the formation of off-stoichiometric B2 phase at 19 at.% Ga and a cascade of A2 → B2 → DO_3 congruent orderings in a single-phase state at 21 at.% Ga. The following decomposition develops mostly via heterogeneous nucleation of the Ga-rich phase on antiphase boundaries (APBs) that serve as nucleation sites.

The color scheme used to visualize the occupation probabilities of Ga atoms is as follows. If the occupation probability of Ga, $n(\mathbf{r})$, is close to 1, then this site is shown in black. If $n(\mathbf{r})$ is close to 0, and thus the occupation probability of Fe is close to 1, then this site is white. In the intermediate cases of $0 < n(\mathbf{r}) < 1$, the probabilities are shown as a shade of gray (a higher occupation probability $n(\mathbf{r})$ by a Ga atom corresponds to a darker shade of gray). The unit cells of the B2 and $D0_3$ crystal structures are shown in Fig. 5.

As follows from Fig. 5, if we want to visualize the distribution $n(\mathbf{r})$ directly and distinguish the B2 and DO_3 order, then we have to simultaneously visualize $n(\mathbf{r})$ in the two nearest (0 0 1) bcc planes. In Fig. 5, the B2 structure is described by an alternating sequence of the $(0\ 0\ 1)_{bcc}$ planes filled by either Ga or Fe. These planes are shown on the right of Fig. 5b. On the other hand, the DO_3 structure is described by a different alternating sequence of (0 0 1) bcc planes: planes homogeneously occupied by Fe have the nearest plane whose sites filled by an equal number of Fe and Ga atoms in an ordered fashion (on the left of Fig. 5a). There are two types of antiphase domains and corresponding antiphase boundaries (APBs) in the $D0_3$-type ordered structure. They are characterized by the $a/4\langle 1\ 1\ 1\rangle$ and $a/2\langle 1\ 0\ 0\rangle$ antiphase shifts where a is DO_3 lattice parameter. The former exist in both the B2-type and the $D0_3$-type ordered structures, whereas the latter exists only in the DO_3-type ordered structure. To visualize the local value of the long-range order parameters (l.r.o.) $x(\mathbf{r})$ and $y(\mathbf{r})$ and to distinguish the different translation variants (antiphase domains) of B2 and DO_3 ordered structures, different colors were used. A change of x/x_{max} from -1 to 1 is indicated by a change in colors from red to blue. The value $x/x_{max} = 0$ (the l.r.o. parameter changes sign) is shown in white. The change of y/y_{max} from -1 to 1 is indicated by a change in color from pink to green and $y/y_{max} = 0$ is shown in white.

Figs. 6 and 7 illustrate the microstructure evolution of the Fe–Ga alloy at the composition $c = 0.19$ and for reduced times $t^* = 0.26$, $t^* = 1.0$, $t^* = 2.1$ and $t^* = 5.1$, at both the atomic-scale and at coarse-grained resolution. Changes of $n(\mathbf{r})$ from 0 to 1 are indicated by different shades of gray and vary from white to black correspondingly.

It can be seen in Figs. 6a and 7a that the initial stages of equilibration of the quenched disordered A2 phase is an ordering. Since $y(\mathbf{r})/y_{max} = 0$ but $x(\mathbf{r})/x_{max} \neq 0$ at $t^* = 0.26$ and $t^* = 1$ (see the bottom row). This ordering produces the transient off-stoichiometric B2 phase in a single-phase state. At this stage the composition of the

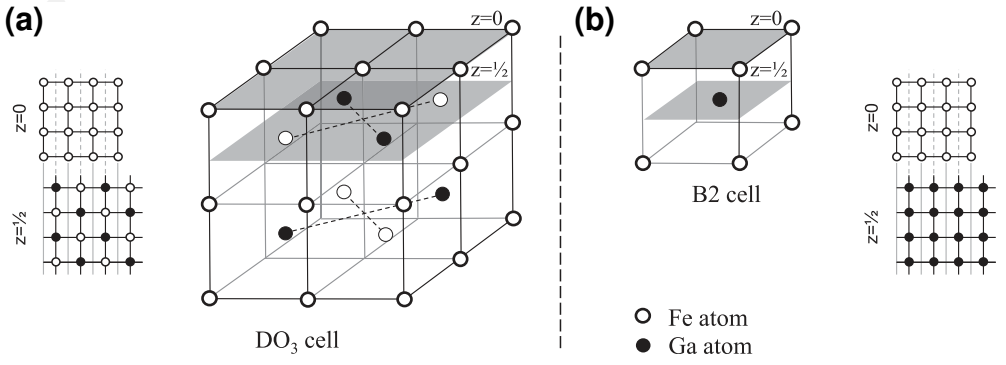

Fig. 5. Unit cells of the DO_3 (a) and B2 (b) ordered structures. On left of (a) and on right of (b) are two nearest $(0\ 0\ 1)_{bcc}$ planes with corresponding distributions of Ga and Fe atoms.

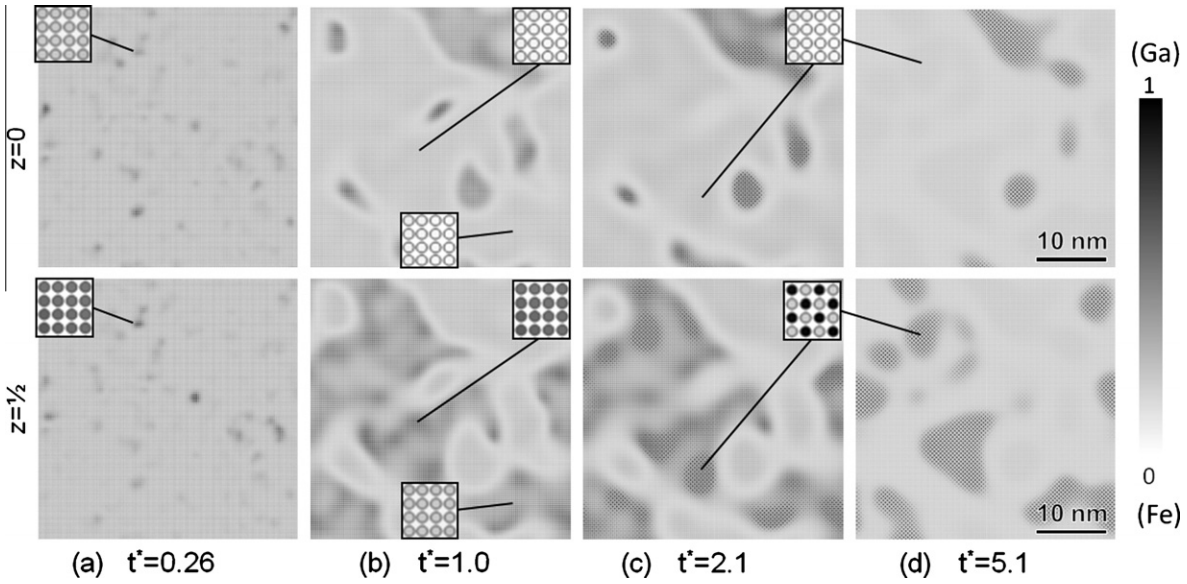

Fig. 6. Microstructural evolution of the system at $c_{Ga} = 0.19$ at 550 °C. The two horizontal rows are images of the microstructures of a region of the material in the two nearest $(0\,0\,1)_{bcc}$ planes with the coordinates, $z = 0$ and $z = 1/2$, along the [0 0 1] direction. The images are visualized values of occupation probability of Ga atoms, n(r), at the reduced times: (a) $t^* = 0.26$, (b) $t^* = 1.0$, (c) $t^* = 2.1$ and (d) $t^* = 5.1$. The images of each column are related to the same time. The insets are magnified images of distribution, $n(\mathbf{r})$, in the regions indicated by the straight lines. They identify the phases in the upper row of images ($z = 0$); the insets visualize the magnified atomic structures in the "white" regions. They show that the bcc lattice sites of this plane in these regions are preferentially occupied by Fe atoms with the same probability. The insets in the bottom row of images ($z = 1/2$) visualize the magnified atomic structures within "gray" regions of the B2 phase and darker ordered regions of the DO_3 phase (compare the insets with unit cell sections in Fig. 5).

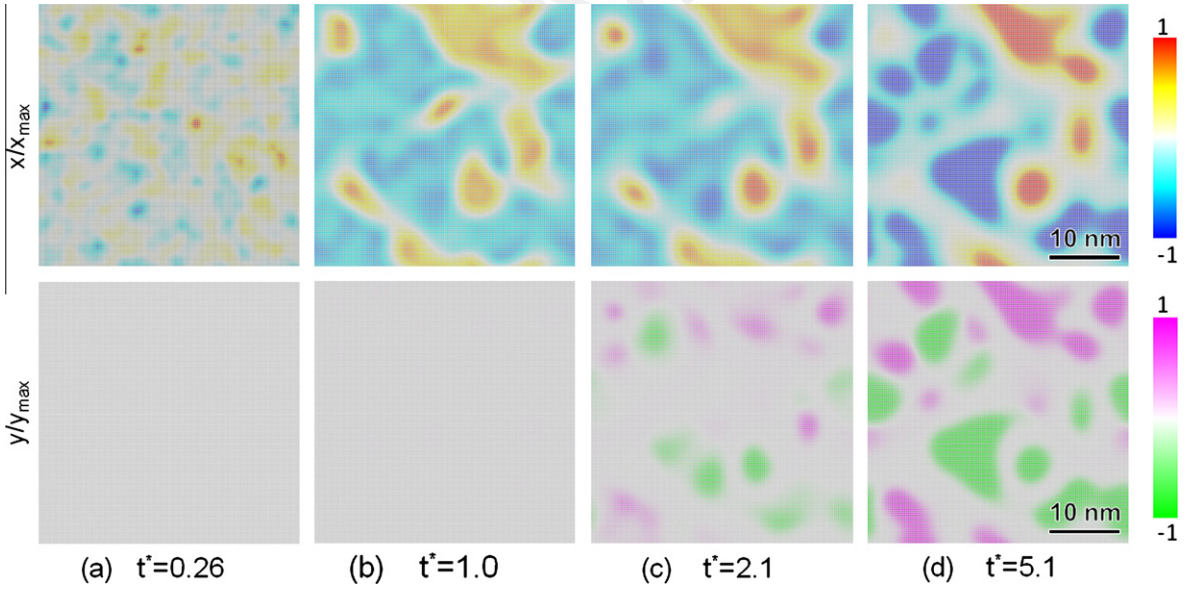

Fig. 7. The microstructure evolution shown in Fig. 6 ($c = 0.19$ and $T = 550$ °C) visualized by the values of the l.r.o. parameters $x(\mathbf{r})/x_{max}$ (upper row) and $y(\mathbf{r})/y_{max}$ (bottom row) in the $(0\,0\,1)_{bcc}$ planes at different reduced times: (a) $t^* = 0.26$, (b) $t^* = 1.0$, (c) $t^* = 2.1$ and (d) $t^* = 5.1$. The l.r.o. parameters are defined by Eq. (6). The positive and negative values of the l.r.o. parameters correspond to different B2 and DO_3 antiphase domains.

ordered domain is very close to the mean concentration of alloy. Therefore, the atomic structure evolution is a congruent ordering up to $t^* \sim 1$. The structure at this stage consists of two types (blue and yellow) antiphase nanodomains of the off-stoichiometric B2 phase, which are distinguished by the sign of $x(\mathbf{r})/x_{max}$ (see two top images at $t^* = 0.26$ and $t^* = 1$ domains). The size of these nanodomains is ~3–5 nm.

The blue and yellow domains in Fig. 7a and b are separated by the APB boundaries, the geometry of which is determined by the condition, $x(\mathbf{r})/x_{max} = 0$, wherein the value of $x(\mathbf{r})/x_{max}$ changes sign and thus assumes zero

value. As follows from Eq. (4), a region where $x = y = 0$ describes the A2 phase with the bcc structure. Therefore APB boundaries are in fact layers of the disordered A2 phase.

The APBs play a role of the nucleation sites for the disordered A2 phase. A depletion of the APB layers by Ga atoms brings the composition of the layers closer to the equilibrium composition of the A2 phase. As a result, the APB boundaries are transformed into layers of the disordered A2 phase (light gray) separating out-of-phase antiphase nanodomains of the B2 phase. A growth of the Ga-poor A2 phase leads to an increase in the composition of Ga atoms in the B2 phase domains (high level of gray in Fig. 6b) in the process of the further separation of composition between the A2 and B2 phases. Fig. 7b demonstrates that at this stage the local order parameter, which is proportional to the amplitude x of the concentration wave with the wave vector $\mathbf{k}_0 = \frac{2\pi}{a}(1\,1\,1)$, increases. It should be noted that the local order parameter $y(\mathbf{r})$, which is proportional to the amplitude of the concentration wave with the wave vector $\mathbf{k}_1 = \frac{2\pi}{a}\left(\frac{1}{2}\,\frac{1}{2}\,\frac{1}{2}\right)$, is zero at this stage of evolution. This indicates that the DO_3 ordered phase has not yet formed. At $t^* = 2.1$, the increasing composition of the Ga-rich regions of B2 phase eventually reaches the value corresponding to the B2/DO_3 boundary on the diffusionless phase diagram in Fig. 3 at the modeling temperature $T = 550$ °C (a point of intersection of the horizontal line corresponding to $T = 550$ °C with the line of the B2/DO_3 boundary). This is the composition of the branching point (second-order transition) in Fig. 2. The Ga-rich B2 precipitates then undergo a spontaneous B2 → DO_3 ordering. This process is illustrated by Figs. 6c and 7c indicating formation of nanodomains of DO_3 phases within the Ga-rich domains of the B2 phase. Figs. 6d and 7d show that the Ga-rich B2 phase eventually completely transforms to the DO_3 phase, and the system becomes a mixture of equilibrium A2 + DO_3 phases.

The microstructure development at composition, $c = 0.21$, is different. This composition is chosen because, as follows from Fig. 3 (right vertical arrow), the equilibration at this composition is expected to occur along a different transformation path than at $c = 0.19$: it should also involve the B2 → DO_3 congruent ordering that is absent at $c = 0.19$. To check whether this is really the case and clarify details of the transformation, we performed the modeling of the same isothermal "annealing" at $c = 0.21$. The results shown in Figs. 8 and 9 demonstrate that the transformation path at this composition is indeed different. Although the initial stage of equilibration at $c = 0.21$ is also the A2 → B2 congruent ordering, the DO_3 ordered phase forms earlier than in the alloys with $c = 0.19$. It already forms at the reduced time $t^* = 1.0$. At time $t^* = 2.1$ the system reaches the A2 + DO_3 two-phase state dictated by the equilibrium phase diagram. As follows from Figs. 8d and 9d, this stage is followed by a coarsening of DO_3 precipitates.

To compare our simulation results with experimental high-resolution transmission electronic microscopy (HRTEM) images [9], we used the same image-processing procedure as in Refs. [8,9] applying it to our simulated microstructures for Fe–19 at.% Ga alloy. Fig. 10 shows our simulated HRTEM images obtained at different

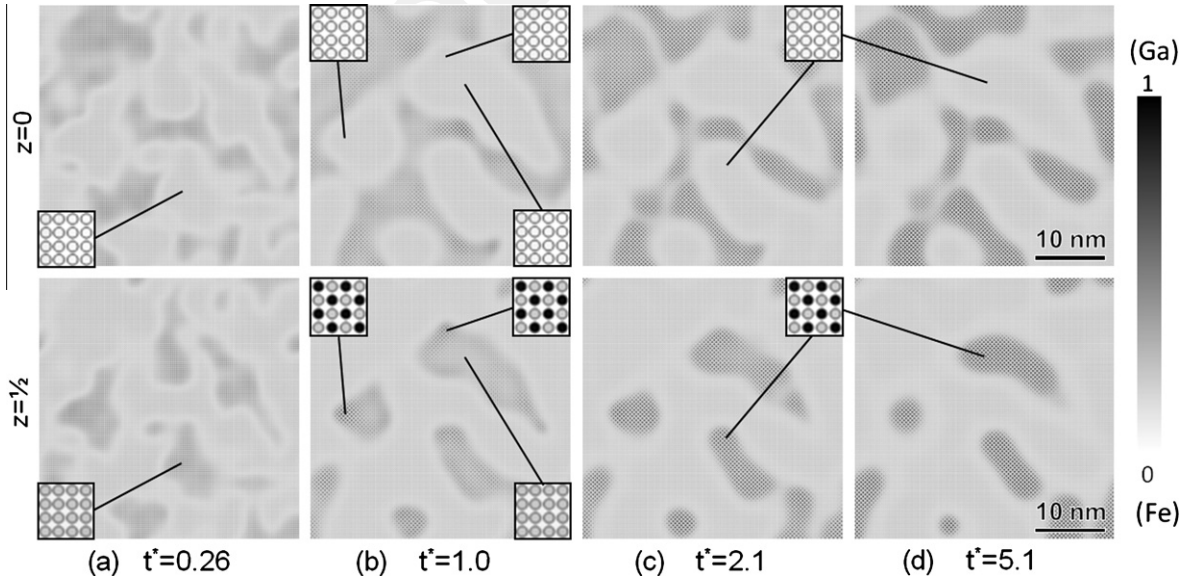

Fig. 8. Microstructural evolution of the system at $c = 0.21$ and 550 °C. Two horizontal rows of figures are images of the microstructures in the two nearest $(0\,0\,1)_{bcc}$ planes with coordinates, $z = 0$ and $z = 1/2$, along the [0 0 1] direction. The images are visualization of values of occupation probability of Ga atoms, $n(\mathbf{r})$, at different reduced times: (a) $t^* = 0.26$, (b) $t^* = 1.0$, (c) $t^* = 2.1$ and (d) $t^* = 5.1$. The images of each column are related to the same time. The insets are magnified images of distribution, $n(\mathbf{r})$, in the regions indicated by the straight lines. The insets identify the phases. In the upper row of images ($z = 0$), they visualize the magnified atomic structures in "white" regions. They show that bcc lattice sites of this plane in these regions are preferentially occupied by Fe atoms with the same probability. The insets in the bottom row of images ($z = 1/2$) visualize the magnified atomic structures within "gray" regions of the B2 phase and darker ordered regions of the DO_3 phase (compare the insets with unit cell sections in Fig. 5).

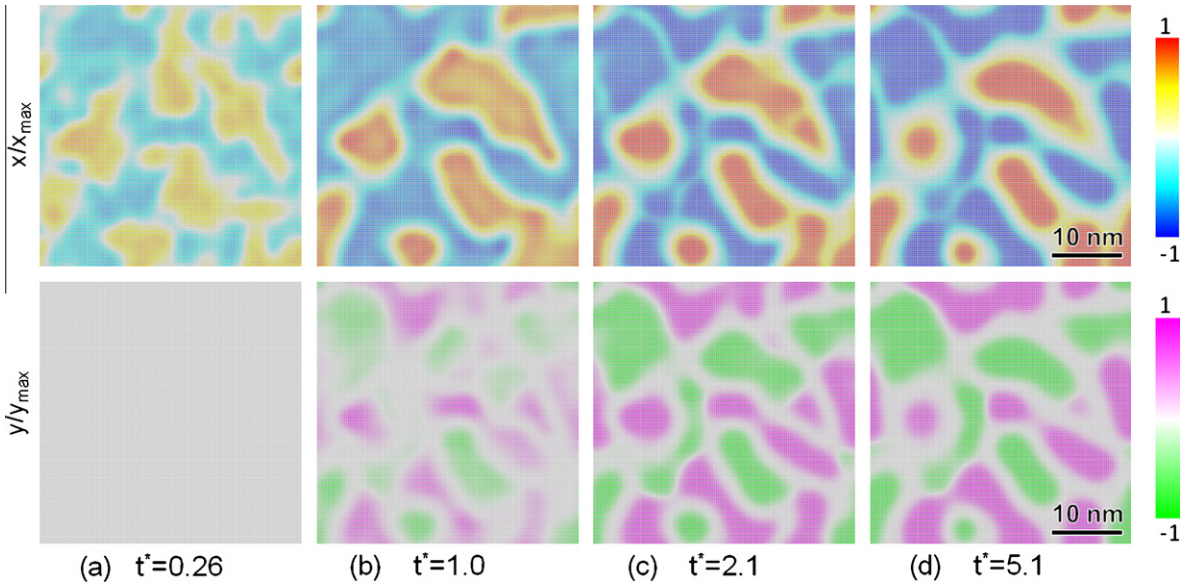

Fig. 9. The microstructure evolution shown in Fig. 8 ($c = 0.21$ and $T = 550$ °C) is visualized by the values of the l.r.o. parameters $x(\mathbf{r})/x_{max}$ (upper row) and $y(\mathbf{r})/y_{max}$ (bottom row) in the $(0\ 0\ 1)_{bcc}$ planes at different reduced times: (a) $t^* = 0.26$, (b) $t^* = 1.0$, (c) $t^* = 2.1$ and (d) $t^* = 5.1$. The l.r.o. parameters are defined by Eq. (6). The positive and negative values of the l.r.o. parameters correspond to different B2 and DO_3 antiphase domains.

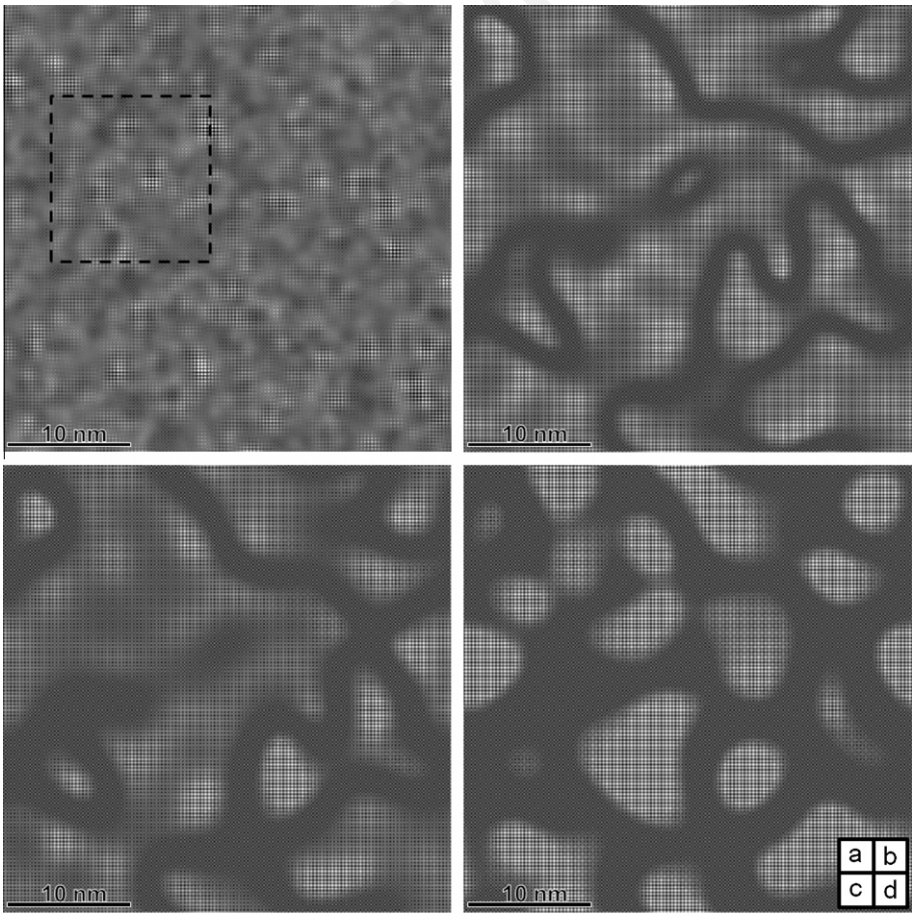

Fig. 10. Simulated images mimicking HRTEM pictures for Fe–19 at.% Ga alloy at 550 °C at different reduced times: (a) $t^* = 0.26$, (b) $t^* = 1.0$, (c) $t^* = 2.1$ and (d) $t^* = 5.1$. The simulated images were obtained using the same procedure that was employed in Ref. [9] to obtain the real HRTEM images.

reduced times: $t^* = 0.26$, $t^* = 1.0$, $t^* = 2.1$ and $t^* = 5.1$. In this figure the regions with the darker contrast indicate the ordered domains of the primary B2 ordering. The almost uniformly gray area corresponds to the disordered A2 phase. The Fig. 10a shows that the nonstoichiometric B2 single-phase state already starts to decompose at $t^* = 0.26$. As we discussed previously, at this stage the size of B2 nanodomains is ~5 nm. As seen from Fig. 10b (reduced time $t^* = 1.0$), the B2 congruently ordered domains are separated by the APBs that are already wetted by the disordered A2 phase. The dashed inset shown in Fig. 10a is enlarged in Fig. 11. The observed HRTEM image [9] (left image) is compared with the simulated one (right image). It should be noted that the ordered domains of the B2 phase observed on the HRTEM and calculated images are comparable in size and topology. As follows from the previous images, the heterogeneous high-contrast zones in Fig. 10c are emerging DO_3 precipitates. The homogeneous contrast zones in Fig. 10d are well-formed DO_3 precipitates embedded into the equilibrium A2 phase matrix.

To provide overall rather than local characterization of these transformations, we also compared the diffraction intensities of superlattice reflections generated by the B2 and DO_3 phases. These intensities were calculated considering a diffraction of the entire system at different evolution times calculated using the kinematic theory of diffuse scattering [26,18].

The B2 and DO_3 ordered phases produce superlattice diffraction peaks in positions related to the wave vectors of the concentration waves, $\mathbf{k}_0 = \frac{2\pi}{a}(1\,1\,1)$ and $\mathbf{k}_1 = \frac{2\pi}{a}\left(\frac{1}{2}\,\frac{1}{2}\,\frac{1}{2}\right)$, generating these ordered structures (see Eq. (4))—in fact, superlattice reflections arise at all equivalent reciprocal space points that are distinguished from the (1 1 1) and $\left(\frac{1}{2}\,\frac{1}{2}\,\frac{1}{2}\right)$ points by a fundamental reciprocal lattice vector. In particular, the B2 phase produces superlattice reflections in positions related to the (1 1 1) point, whereas the DO_3 phase produces reflections at the same points as

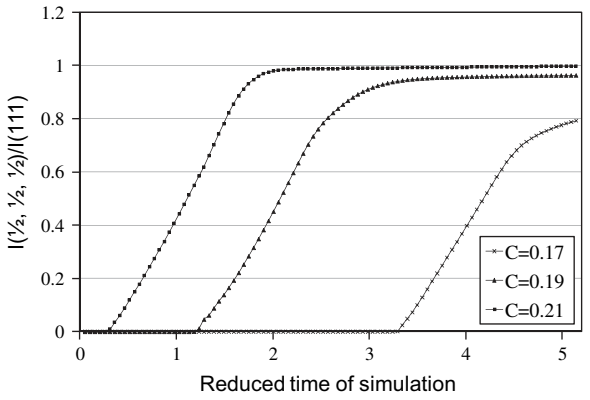

Fig. 12. Intensity ratio $I\left(\frac{1}{2}\,\frac{1}{2}\,\frac{1}{2}\right)/I(1\,1\,1)$ as a function of reduced simulation time for $c = 0.17$, 0.19 and 0.21. The calculated intensities, $I\left(\frac{1}{2}\,\frac{1}{2}\,\frac{1}{2}\right)$ and $I(1\,1\,1)$, are maximum values of intensity in small spherical volumes centered on the points $I\left(\frac{1}{2}\,\frac{1}{2}\,\frac{1}{2}\right)$ and $I(1\,1\,1)$ of the reciprocal lattice.

B2 phase plus reflections in the points related to the $\left(\frac{1}{2}\,\frac{1}{2}\,\frac{1}{2}\right)$ points. The maximum of intensity of superlattice reflections generated by the B2 phase is proportional to the squared l.r.o. parameter, $I(1\,1\,1) \sim x^2 V_{B2}^2$, where V_{B2} is the volume of the B2 phase. The intensity of the superlattice reflections generated by the DO_3 phase is proportional to the squared l.r.o. parameter, $I\left(\frac{1}{2}\,\frac{1}{2}\,\frac{1}{2}\right) \sim y^2 V_{DO_3}^2$, where V_{DO_3} is the volume of the DO_3 phase. A ratio of intensities of $\left(\frac{1}{2}\,\frac{1}{2}\,\frac{1}{2}\right)$ and (1 1 1) reflections, $I\left(\frac{1}{2}\,\frac{1}{2}\,\frac{1}{2}\right)/I(1\,1\,1) \sim y^2 V_{DO_3}^2 / x^2 V_{B2}^2$, is an indicator of the DO_3 phase.

The $I\left(\frac{1}{2}\,\frac{1}{2}\,\frac{1}{2}\right)/I(1\,1\,1)$ ratio was calculated by applying the kinematic theory of diffraction [18,26] to the simulated atomic distributions of the ordered phases. The atomic distribution at different times is obtained by our modeling and is presented in Fig. 12. The intensity at each point is calculated as the maximum value of the intensity in a small spherical volume centered on this point. The DO_3 phase is absent and the B2 phase is present if the ratio is equal to 0 and $x \neq 0$. The presence of the DO_3 phase is indicated by a nonvanishing ratio, $I\left(\frac{1}{2}\,\frac{1}{2}\,\frac{1}{2}\right)/I(1\,1\,1)$. A ratio equal to 1

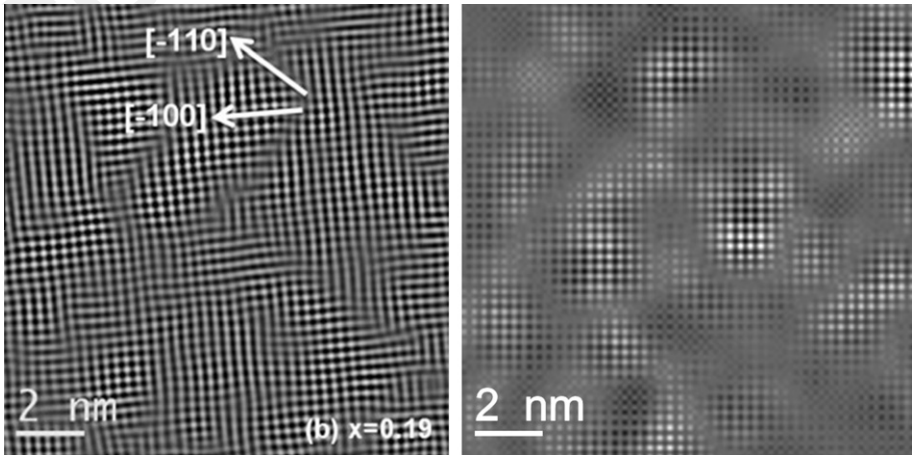

Fig. 11. Comparison between observed [9] (left) and simulated (right) HRTEM images for Fe–19 at.% Ga alloy. The simulation image corresponds to the amplification of the dashed area in Fig. 10a.

indicates that the system forms a DO_3 single-phase state with the maximum order parameter permitted by its composition. Intermediate values of the ratio, $0 < I\left(\frac{1}{2}\,\frac{1}{2}\,\frac{1}{2}\right)/I(1\,1\,1) < 1$, either imply that the alloy forms the single-phase partially ordered DO_3 phase or that it is a two-phase mixture of DO_3 and B2 phase, or DO_3 and A2 phases.

Fig. 12 clearly demonstrates that formation of the transient B2 phase at compositions $c = 0.17$, $c = 0.19$ and $c = 0.21$ occurs by via A2 → B2 ordering prior to formation of the more stable DO_3 phase.

Equilibration at a Ga composition of $c = 0.19$ (curve marked by triangles) develops in three stages. The first stage corresponds to the ratio $I\left(\frac{1}{2}\,\frac{1}{2}\,\frac{1}{2}\right)/I(1\,1\,1) = 0$ when $y/y_{\max} = 0$ and $x/x_{\max} \neq 0$ at $t^* < 1.3$. This indicates the A2 → B2 ordering at $0 < t^* < 1.3$. The Figs. 7a and 10a show that this ordering reaction initially develops congruently. The second stage starts at $t^* \sim 1.3$ when the ratio $I\left(\frac{1}{2}\,\frac{1}{2}\,\frac{1}{2}\right)/I(1\,1\,1)$ assumes nonzero values. The latter is a fingerprint of the formation of the DO_3 phase.

The third stage develops at $t^* > \sim 3$ when the intensity ratio reaches a plateau where the intensity ratio is close to unity. The equilibration process at this stage is completed, and the system transforms into the equilibrium mixture of the A2 and DO_3 phases. The process involved the isostructural B2 → B2′ + B2″ decomposition into a mixture of Ga-poor B2′ and Ga-rich B2″ phase, which was followed by the B2 → A2 disordering of the B2′ phase and the B2″ → A2 + DO_3 decomposition of the B2″ phase.

As was expected, the transformation pathway at $c = 0.21$ and $T = 550$ °C turns out to be different. It follows from Figs. 8 and 9 that the transformation develops in three stages.

The first stage is the direct A2 → B2 congruent ordering—the direct A2 → DO_3 congruent ordering at this composition is forbidden by the thermodynamics since the temperature of such an ordering is significantly lower than 550 °C. The DO_3 phase forms only at the second stage at $t^* > \sim 0.3$ as a result of the B2 → DO_3 secondary congruent ordering. It occurs when the increasing l.r.o. parameter of the primary ordered B2 phase, x, reaches the critical value providing the secondary B2 → DO_3 congruent ordering at the temperature of annealing, $T = 550$ °C. The details of this ordering for the composition $c = 0.21$ follow from the simulated local images in Figs. 8a,b and 9a,b. These results are in agreement with the cascade of bcc → B2 → DO_3 congruent orderings that was predicted in Section 2 using general thermodynamic arguments illustrated by Figs. 2 and 3. The atomic structure and two-phase morphology of the third stage, the DO_3 → A2 + DO_3 decomposition, is illustrated by Figs. 8c and 9c.

5. Discussion

Interest in Fe–Ga alloys has been increased by the discovery of GM within the range 17–19.5 at.% Ga. A history-dependence and the correlation of this property with the phase diagram are indicative that the special magnetomechanic properties of the system are associated with structural transformations. The known phase diagram of Fe–Ga is complicated by the existence of three thermodynamically competing ordered phases and decomposition. TEM studies [6–10] have demonstrated that a Fe–Ga alloy within this range is not the homogeneous disordered bcc A2 phase, but rather is a coherent dispersion of nanoscale clusters. A polarized neutron diffraction study under an applied magnetic field [27] showed that these clusters are tetragonal and that the orientation of their tetragonal lattice is changed by the application of a magnetic field—the effect predicted by the KV model of extrinsic model of GM [4,5].

Even prior to this work, there were compelling reasons to believe that the equilibration of Fe–Ga alloy within the investigated composition range develops via a cascade of ordering and decomposition reactions. Given a well-established dependence of magnetostriction on thermal history as well as observations of nanoscale heterogeneities, any nanoscale transformation in the system producing structurally and compositional inhomogeneous states [6–10] is of great interest.

To clarify structural aspect of complex phase transformations in Fe–Ga magnetostrictive alloys, we carried out a computational prototyping of atomic-scale diffusion at compositions of 19 and 21 at.% Ga at a typical temperature $T = 550$ °C. It was shown that the transformations do not develop in accordance with the textbook scenario of nucleation and growth of the equilibrium DO_3 phase within the A2 (bcc) matrix. Instead, they develop via a cascade of ordering and decomposition reactions producing transient phases along the pathway to the equilibrium of the two-phase (A2 + DO_3) state.

One reason for this complexity is the disparity between rates of congruent ordering developing without changes in composition and decomposition. The ordering is a much faster process because it requires atomic diffusion over distances comparable with the interatomic distances. On the other hand, the decomposition is much slower because it develops via atomic migration over comparatively long distances comparable with distances between precipitates. Equilibration of the supersaturated solid solution under these circumstances initially develops by the fastest available mode, and this mode is a congruent ordering maintaining compositional homogeneity of the crystal (with accuracy of effect produced by employed random noise mimicking thermal fluctuations [13]). The diffusionless phase diagram with the A2, B2 and DO_3 phases describing the congruent ordering is shown in Fig. 3. Because the diagram is diffusionless, the phase fields on this diagram are separated by boundary lines rather than existing as a two-phase field as is required by the Gibbs phase rule. The lines are the locus of points where the free energies of the neighboring phases are equal at the same composition. After a system reaches "diffusionless equilibrium", further evolution to the two-phase equilibrium occurs by

decomposition. The two-phase field equilibrium after decomposition is completed is described by Fig. 4.

In the case of the Fe–Ga alloys, congruent ordering is complicated because the alloys have two lines of congruent ordering, the bcc/B2 and B2/DO_3 lines. The further equilibration of the congruently ordered B2 or DO_3 nonstoichiometric phases occurs via their decomposition. Our modeling demonstrates a sequence of transient microstructures formed along the transformation path, and this sequence is determined by the thermodynamics of the system and the disparity in the rates of the bcc → B2, B2 → DO_3 ordering and decomposition. The dependence of the transformation path on the thermodynamics is determined by the position of the representative (T, c) point of isothermal annealing with respect to lines of the congruent equilibrium on the diffusionless phase diagram shown in Fig. 3. Given the fact that the high magnetostrictive states are heterogeneous, any specifics of the microstructure transformation within the T–c range, where these states are observed, is of a special interest [6–10]. The use of the atomic-scale model and the ADF theory [16–18] allowed us to obtain images of nanoscale microstructures formed within the T–c range of interest at atomic-scale "resolution". In particular, we considered the equilibration kinetics at $T = 550$ °C and Ga compositions of $c = 0.19$ and $c = 0.21$.

The main result of our modeling is that the congruent ordering in Fe–Ga produces the transient phase with the B2 ordered structure although B2 phase does not exist on the phase diagram at a temperature of 550 °C and below (Fig. 1). The latter is a key point for understanding the GM if we assume that it this caused by the magnetic field-induced reorientation of tetragonally transformed nanoprecipitates of the B2 phase—the tetragonally distorted B2 phase is in fact the L10 phase.

Although the contribution of the elastic strain generated by the crystal lattice misfit between the phases was taken into consideration, it turned out to be insufficient to appreciably affect the microstructure morphology. One of the reasons for that is the comparatively small misfit between the matrix and precipitate phase. The other reason is the small precipitate size. As follow from our simulation, a typical size is ~5–10 nm. Since this size is small and the strain energy is proportional to the volume of a precipitate, we have a situation wherein the strain energy, which is volume dependent, is significantly smaller than the interfacial energy, and thus this is the interface energy that determines morphology of precipitates. Observation of the {1 0 0} faceting only for large particles of the DO_3 ordered phase (~100 nm) [28], which is typical for the cases wherein the strain energy contribution is significant, is in agreement with this interpretation.

To compare our results with experimental data, we also have to be sure that the rate of the decomposition and ordering in Fe–Ga alloys at 550 °C is sufficient to produce the effects described by modeling. This can be done by the estimation of a relation between the reduced time used in the modeling and the real time at the temperature of isothermal annealing. To do this, we used the Ikeda et al. data [3]. They observed formation of ordered precipitates 300 nm in size after 3 days of aging at 550 °C. On the other hand, our modeling at the same temperature and reduced time $t^* = 5.1$ shows the formation of DO_3 phase precipitates with a medium size of 8 nm. By assuming a relation $R^2 \sim Dt.$ between the size of a precipitate, R, and growth time, t, and the same diffusivity, D, for nanosized particles and particles 300 nm in size, we have a proportionality $(300/8)^2 \sim (3 \times 24 \times 3600\ \mathrm{s/t_o})$ where to is the actual annealing time resulting in the formation of 8 nm precipitates (it corresponds to the reduced time $t^* = 5.1$). This relation gives an estimate of $t_o \sim 3$ min for the reduced time $t^* = 5.1$ required for formation of nanoprecipitates at 550 °C. Therefore, our estimate for the reduced time at this temperature is ~35 s. This diffusion rate is sufficient to produce B2 ordered nanoprecipitates for most cases of cooling.

Therefore, our prototyping of the equilibration kinetics in Fe–19 at.% Ga demonstrates that this does not develop by a conventional mechanism of nucleation and growth of the equilibrium DO_3 phase within the supersaturated bcc matrix of the A2 phase. Rather it has three structurally and morphologically distinctive stages.

The first stage (arrow 1 in Fig. 2) is congruent A2 → B2 ordering (Figs. 6a and 7a). This ordering produces nonstoichiometric transient B2 phase (B2) phase in a single-phase state (Figs. 6a and 7a). APBs of this phase have the locally disordered bcc structure of the A2 phase and thus in fact are built-in nuclei of the A2 phase.

The second stage (arrow 2 in Fig. 2) is decomposition of the nonstoichiometric phase B2 phase into a mixture of the A2 phase and transient Ga-rich B2 phase (B2″), the latter being further gradually enriched by Ga. Therefore, the initial microstructure consists of nanoprecipitates of the transient B2 phase within the A2 matrix. The microstructure forms by wetting APBs of the previously formed nonstoichiometric B2 phase by the disordered A2 phase, thickening of wetted APBs into layers of the A2 phase (Figs. 6b and 7b), and eventually transformation of these layers into A2 matrix. This process is accompanied by migration of Ga atoms from regions adjacent to the wetted APBs to the adjacent newly formed Ga-rich B2″ phase. The equilibration of transient B2 phase occurs by gradual increase of Ga content, which provides a route for the eventual transition to the equilibrium DO_3 phase. The formation of transient B2 phase prior to the equilibrium DO_3 phase is illustrated by Figs. 6b and 7b, and especially by Figs. 6c and 7c.

In the third stage (arrow 3 in Fig. 2), the formation of the DO_3 phase starts when the increasing content of Ga in the B2″ phase reaches the concentration corresponding to the line of the B2/DO_3 diffusionless equilibrium at the annealing temperature (the evolution of the representative point (T, c) of the B2 phase in this process is described by a horizontal line in the phase diagrams in Figs. 3 and

4). When the Ga-rich B2 precipitates reach this composition limit, they undergo B2 → DO_3 congruent ordering and form particles of nonequilibrium DO_3 phase. Further equilibration occurs by Ga enrichment of the DO_3 phase due to migration of Ga atoms from the A2 matrix and eventual attainment of the equilibrium composition in both phases (Figs. 6d and 7d). This multi-stage transformation sequence obtained in our computational modeling is also supported by the general thermodynamic arguments presented in Section 2.

The observations of the maximum of the magnetostriction in Fe–Ga alloys within the 15–19.5 at.% Ga composition range can be easily understood in terms of the KV theory of extrinsic magnetostriction [4,5] and these modeling results. We simply have to assume that nanoprecipitates of the transient cubic B2 phase formed at early stage of annealing undergo the cubic → tetragonal martensitic transformation during cooling of a sample to room temperature and thus become precipitates of the L10 ordered phase. This assumption is consistent with the experimental data reporting that the GM of Fe–Ga alloys is associated with the B2 ordered phase, and the formation of the DO_3 phase is detrimental to the magnetostriction [29]. On the other hand, our computer modeling indicates that the volume fraction of the transient B2 phase is maximum at about 19 at.% Ga. Therefore, the magnetostriction associated with the tetragonally transformed B2 phase, and thus the dependence of its volume fraction on composition (and time), should have a maximum at the same compositions. An observed reduction in magnetostriction with time is also explained by a gradual vanishing of the volume of the transient B2 phase during prolonged annealing, which is obtained in our modeling at $c \approx 0.19$. Our results also explain why a choice of composition of Ga within the two-phase region also reduces the magnetostriction: such a choice increases the volume fraction of the DO_3 phase (and thus decreases the volume of the transient B2 phase).

It should be noted that the original KV model [4,5] assumes that the tetragonal nanoprecipitates are tetragonally transformed precipitates of the cubic DO_3 phase which, in fact, is the tetragonal DO_{22} phase. However, the current modeling results and the experimental data [29] require a slight modification of this assumption. We still have to assume that the tetragonal precipitates are formed by the cubic → tetragonal martensitic transformation of precipitates of the ordered cubic phase upon cooling to room temperature. However, this cubic phase is the transient B2 phase rather than the DO_3 phase. If this is this case, the Bain distortion of the B2 phase produces the ferromagnetic tetragonal L10 phase rather than the DO_{22} phase obtained by the tetragonal distortion of the DO_3 phase and assumed by the KV model. This clarification does not affect the KV mechanism of extrinsic magnetostriction because this is a tetragonality of nanoprecipitates rather than a type of their atomic order that is really important for the KV mechanism. Therefore, according to a modified KV mechanism, the DO_3 phase formed in the ordering is assumed to be cubic at all stages of the system equilibration. The tetragonal phase responsible for the amplified magnetostriction is the transient L10 phase, which is formed by the martensitic B2 → L10 transformation within B2 precipitates upon cooling.

The modeling results also allow us to understand why quenching alloys with $c \sim 17$–19% provides higher magnetostriction than slow cooling. Indeed, if the cooling is sufficiently slow to allow the A2 → B2 congruent ordering, but is too fast for the B2 → DO_3 precipitation, the transformation produces either a congruently ordered B2 phase or Ga-rich B2 nanoparticles embedded into disordered A2 phase. This is the structure obtained at early stages of the simulated annealing. Since the nanoparticles of the B2 phase are assumed to be martensitically transformed and thus are tetragonal nanoparticles of the L10 phase, they should, according to the KV model, provide high values of the magnetostriction. Otherwise, if the cooling is sufficiently slow to allow the B2 → DO_3 decomposition, then the volume of the tetragonally deformed B2 phase is either reduced or vanishes, which is detrimental to the magnetostriction and which is observed.

6. Conclusion

The numerical solution of the ADF kinetic equations shows that the kinetics of equilibration of disordered Fe–Ga alloys at 550 °C develops as a cascade of phase transformations, A2 → B2 → DO_3, including congruent ordering and decomposition. The composition range of these transformations is within the range of the observed GM in Fe–Ga alloys.

At a concentration of 19 at.% Ga the transformation starts as A2 → B2 congruent ordering. The formation of the nonstoichiometric single-phase B2 ordered state is followed by the B2 → B2′ + B2″ isostructural decomposition. The Ga-rich B2″ subsequently decomposes as B2″ → A2 + DO_3. An important detail of this congruent ordering and subsequent precipitation is the formation of Ga-rich B2″ nanoprecipitates ~3–10 nm in size. This size is comparable to the size of precipitates observed in the HRTEM images.

At a concentration of 21 at.% Ga, the decomposition at $T = 550$ °C develops much faster, as a A2 → B2 → DO_3 sequence of two congruent orderings followed by the precipitation of the equilibrium DO_3 phase resulting in the formation of the A2 + DO_3 two-phase equilibrium.

The obtained microstructure evolution can explain the observed maximum in magnetostriction at $c \sim 0.19$ in terms of the KV model by relating this maximum to the maximum of the volume fraction of the transient B2 phase obtained by modeling at $c \approx 0.197$.

The obtained microstructure evolution can also explain the reduction in magnetostriction during prolonged annealing by a gradual disappearance of the transient B2 phase dictated by the thermodynamics.

The microstructures predicted by our computer simulations agree with recent experimental observations on Fe–Ga alloys.

Acknowledgements

A.G.K. and J.B. gratefully acknowledge the support from NSF DMR under the Grant NSF DMR-0704045 and the Office of Naval Research through Grant Nos. MURI-N00014-06-1-0530; H.Z. was partially supported by the PEPS "Champs de Phase cristallin". The parallel computer simulations were performed on the LoneStar in the Texas Advanced Computing Center.

References

[1] Clark AE, Wun-Fogle M, Restorff JB, Lograsso TA, Cullen JR. IEEE Trans Magn 2001;37:2678.
[2] Srisukhumbowornchai N, Guruswamy S. J Appl Phys 2001;90:5680.
[3] Ikeda O, Kainuma R, Ohinuma I, Fukamichi F, Ishida K. J Alloys Compd 2002;347:198.
[4] Khachaturyan AG, Viehland DD. Metal Mater Trans A 2007;38A: 2317.
[5] Khachaturyan AG, Viehland DD. Metal Mater Trans A 2007;38A: 2308.
[6] Liu GD, Liu LB, Liu ZH, Zhang M, Chen JL, Li JQ, et al. Appl Phys Lett 2004;84:2124.
[7] Liu L, Fu S, Liu G, Sun X, Li J. Phys B 2005;365:102.
[8] Bhattacharya S, Jinschek JR, Khachaturyan AG, Cao H, Li JF, Viehland DD. Phys Rev B 2008;77:104107.
[9] Bhattacharya S, Jinschek JR, Li JF, Viehland DD. J Alloys Compd 2010;501:148.
[10] Zhang MC, Gao XX, Jiang HL, Qiao Y, Zhou SZ. J Alloys Compd 2007;431:42.
[11] Warlimont H, Thomas G. Met Sci J 1970;4:47.
[12] Watanabe D, Morita H, Saito H, Ogawa S. J Phys Soc Jpn 1970;29:722.
[13] Chen LQ, Khachaturyan AG. Acta Metall Mater 1991;39:2533.
[14] Khachaturyan AG, Lindsey TF, Morris JW. Metall Trans 1988;19A: 249.
[15] Soffa WA, Laughlin DE. Acta Metall 1989;37:3019.
[16] Khachaturyan AG. Phys Status Solidi (b) 1973;60:9 (review article).
[17] Khachaturyan AG. Ordering in substitutional and interstitial solid solutions. In: Chalmers B, Christian JW, Massalski TB, editors. Progress in Materials Science. Oxford: Pergamon Press; 1978. p. 22:1–22:150.
[18] Khachaturyan AG. The theory of structural transformation in solids. New York: Wiley; 1983.
[19] Khachaturyan AG. Sov Phys Solid State 1967;9:2163.
[20] Khachaturyan AG, Shatalov GA. Sov Phys JEPT 1969;29:557.
[21] Chen LQ, Shen J. Comp Phys Comm 1998;108:147.
[22] Kawamiya N, Adachi K, Nakamura Y. J Phys Soc Jpn 1972;33:1318.
[23] Allen SM, Cahn JW. Acta Metall 1976;24:425.
[24] McLean KO, Smith CS. J Phys Chem Solids 1972;33:279.
[25] Wuttig M, Dai L, Cullen J. Appl Phys Lett 2002;80:1135.
[26] Krivoglaz MA, Ivanov MA, Baryakhtar VG, Moss SC. X-ray and neutron diffraction. New York: Springer; 1995.
[27] Mudivarthi C, Laver M, Cullen J, Flatau AB, Wuttig M. J Appl Phys 2010;107:09A957.
[28] Yasuda HY, Aoki M, Umakoshi Y. Acta Mater 2007;55:2407.
[29] Kumagai A, Fujita A, Fukamichi F, Oikawa K, Kainuma R, Ishida K. J Magn Magn Mater 2004;272:2060.